Supplementary information

Figure S1

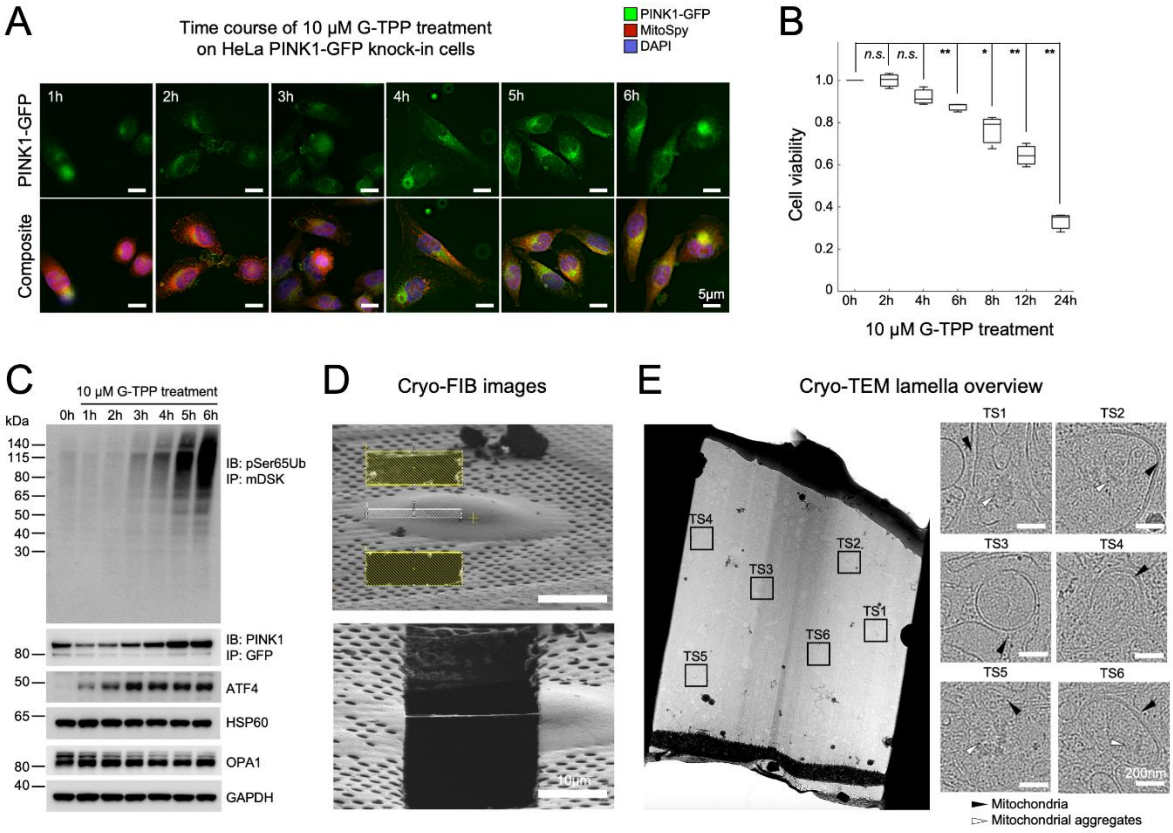
A
Time course of 10 µM G-TPP treatment
on HeLa PINK1-GFP knock-in cells
PINK1-GFP
MitoSpy
DAPI
PINK1-GFP
Composite
1h
2h
3h
4h
5h
6h
5µm
B
Cell viability
n.s.
n.s.
**
*
**
**
0h
2h
4h
6h
8h
12h
24h
10 µM G-TPP treatment
C
10 µM G-TPP treatment
kDa
0h 1h 2h 3h 4h 5h 6h
IB: pSer65Ub
IP: mDSK
IB: PINK1
IP: GFP
ATF4
HSP60
OPA1
GAPDH
D
Cryo-FIB images
E
Cryo-TEM lamella overview
TS1
TS2
TS3
TS4
TS5
TS6
200nm
Mitochondria
Mitochondrial aggregates
F
Control
G
Proteostatic stress
mito
ER
LD
MT
IF
Agg
200 nm
Typical perpendicular cristae
Altered parallel Cristae
Circular cristae
Aggregates
ER Endoplasmatic riticulum
mito Mitochondria
MT Microtubules
IF Intermediate filaments
LD Lipid droplet

Figure S 1: G-TPP treatment induces proteostatic stress in HeLa cells. (**A**) Fluorescence microscopy of PINK1-GFP HeLa cells at time intervals following 10 µM G-TPP treatment. Increasing co-localization of PINK1-GFP with the mitochondrial marker MitoSpy indicates PINK1 stabilization at mitochondria upon proteostatic stress. (**B**) Quantification of cell viability as a function of time following 10 µM G-TPP treatment. Statistical significance of pairwise comparisons was assessed using a two-sample t-test and indicated by: n.s. ($p > 0.05$), * ($p < 0.05$) and ** ($p < 0.01$). N = 3 independent experiments. (**C**) Western blot analysis of the effects of G-TPP treatment on PINK1 accumulation and activation, measured by increased levels of ubiquitin phosphorylation at serine 65 (pSer65Ub). OPA1 band shifts and ATF4 activation serve as additional indicators of mitochondrial stress. (**D**) Ion beam-induced secondary electron images of a HeLa cell vitrified on an EM grid, shown during (top) and after (bottom) cryo-FIB milling. (**E**) Left: cryo-TEM image of a cryo-FIB-milled lamella from a vitrified HeLa cell that underwent 10 µM G-TPP treatment. Boxes mark regions selected for tomographic tilt series (TS) acquisition. Right: Magnified views of the regions of tomographic data acquisition highlighting mitochondria (black arrowheads). In some cases, mitochondrial aggregates (white arrowheads) were readily distinguishable. (**F–G**) Gallery of tomographic slices from untreated control (F) and G-TPP–treated cells under proteostatic stress (G). Cellular structures are annotated in the slices according to the legend at the bottom of the figure.

Figure S2

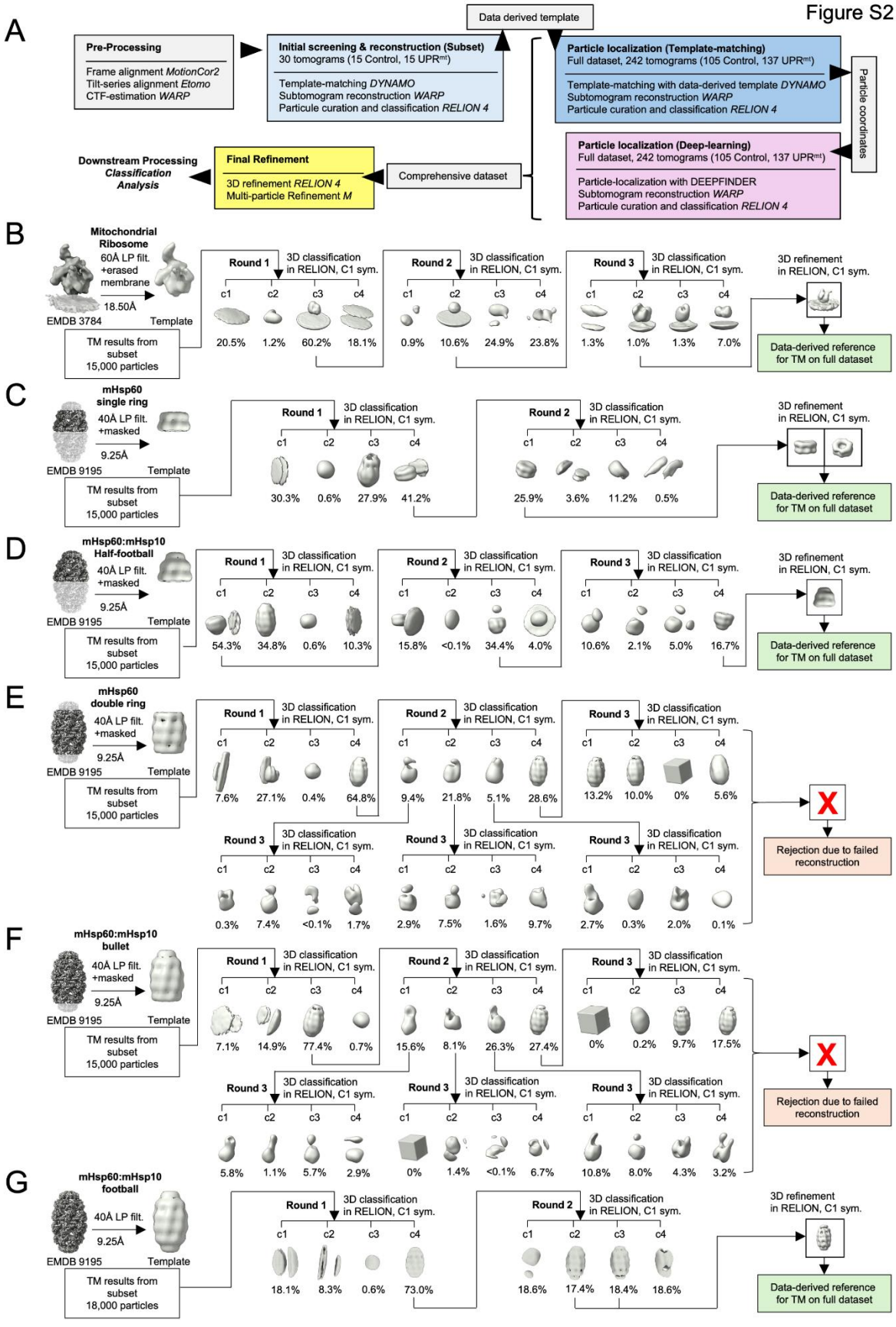
A
Pre-Processing
Frame alignment MotionCor2
Tilt-series alignment Etomo
CTF-estimation WARP
Initial screening & reconstruction (Subset)
30 tomograms (15 Control, 15 UPRmt)
Template-matching DYNAMO
Subtomogram reconstruction WARP
Particule curation and classification RELION 4
Data derived template
Particle localization (Template-matching)
Full dataset, 242 tomograms (105 Control, 137 UPRmt)
Template-matching with data-derived template DYNAMO
Subtomogram reconstruction WARP
Particule curation and classification RELION 4
Particle coordinates
Particle localization (Deep-learning)
Full dataset, 242 tomograms (105 Control, 137 UPRmt)
Particle-localization with DEEPFINDER
Subtomogram reconstruction WARP
Particule curation and classification RELION 4
Downstream Processing
Classification
Analysis
Final Refinement
3D refinement RELION 4
Multi-particle Refinement M
Comprehensive dataset
B
Mitochondrial Ribosome
60Å LP filt.
+erased membrane
18.50Å
EMDB 3784
Template
TM results from subset 15,000 particles
Round 1
3D classification in RELION, C1 sym.
c1 c2 c3 c4
20.5% 1.2% 60.2% 18.1%
Round 2
3D classification in RELION, C1 sym.
c1 c2 c3 c4
0.9% 10.6% 24.9% 23.8%
Round 3
3D classification in RELION, C1 sym.
c1 c2 c3 c4
1.3% 1.0% 1.3% 7.0%
3D refinement in RELION, C1 sym.
Data-derived reference for TM on full dataset
C
mHsp60 single ring
40Å LP filt.
+masked
9.25Å
EMDB 9195
Template
TM results from subset 15,000 particles
Round 1
3D classification in RELION, C1 sym.
c1 c2 c3 c4
30.3% 0.6% 27.9% 41.2%
Round 2
3D classification in RELION, C1 sym.
c1 c2 c3 c4
25.9% 3.6% 11.2% 0.5%
3D refinement in RELION, C1 sym.
Data-derived reference for TM on full dataset
D
mHsp60:mHsp10 Half-football
40Å LP filt.
+masked
9.25Å
EMDB 9195
Template
TM results from subset 15,000 particles
Round 1
3D classification in RELION, C1 sym.
c1 c2 c3 c4
54.3% 34.8% 0.6% 10.3%
Round 2
3D classification in RELION, C1 sym.
c1 c2 c3 c4
15.8% <0.1% 34.4% 4.0%
Round 3
3D classification in RELION, C1 sym.
c1 c2 c3 c4
10.6% 2.1% 5.0% 16.7%
3D refinement in RELION, C1 sym.
Data-derived reference for TM on full dataset
E
mHsp60 double ring
40Å LP filt.
+masked
9.25Å
EMDB 9195
Template
TM results from subset 15,000 particles
Round 1
3D classification in RELION, C1 sym.
c1 c2 c3 c4
7.6% 27.1% 0.4% 64.8%
Round 2
3D classification in RELION, C1 sym.
c1 c2 c3 c4
9.4% 21.8% 5.1% 28.6%
Round 3
3D classification in RELION, C1 sym.
c1 c2 c3 c4
13.2% 10.0% 0% 5.6%
Round 3
3D classification in RELION, C1 sym.
c1 c2 c3 c4
0.3% 7.4% <0.1% 1.7%
Round 3
3D classification in RELION, C1 sym.
c1 c2 c3 c4
2.9% 7.5% 1.6% 9.7%
Round 3
3D classification in RELION, C1 sym.
c1 c2 c3 c4
2.7% 0.3% 2.0% 0.1%
X
Rejection due to failed reconstruction
F
mHsp60:mHsp10 bullet
40Å LP filt.
+masked
9.25Å
EMDB 9195
Template
TM results from subset 15,000 particles
Round 1
3D classification in RELION, C1 sym.
c1 c2 c3 c4
7.1% 14.9% 77.4% 0.7%
Round 2
3D classification in RELION, C1 sym.
c1 c2 c3 c4
15.6% 8.1% 26.3% 27.4%
Round 3
3D classification in RELION, C1 sym.
c1 c2 c3 c4
0% 0.2% 9.7% 17.5%
Round 3
3D classification in RELION, C1 sym.
c1 c2 c3 c4
5.8% 1.1% 5.7% 2.9%
Round 3
3D classification in RELION, C1 sym.
c1 c2 c3 c4
0% 1.4% <0.1% 6.7%
Round 3
3D classification in RELION, C1 sym.
c1 c2 c3 c4
10.8% 8.0% 4.3% 3.2%
X
Rejection due to failed reconstruction
G
mHsp60:mHsp10 football
40Å LP filt.
9.25Å
EMDB 9195
Template
TM results from subset 18,000 particles
Round 1
3D classification in RELION, C1 sym.
c1 c2 c3 c4
18.1% 8.3% 0.6% 73.0%
Round 2
3D classification in RELION, C1 sym.
c1 c2 c3 c4
18.6% 17.4% 18.4% 18.6%
3D refinement in RELION, C1 sym.
Data-derived reference for TM on full dataset

Figure S 2: Cryo-ET particle picking workflow and localization of mitochondrial protein complexes by template matching. (**A**) Schematic overview of the processing strategy. After initial preprocessing, mitochondrial complexes were identified and their relative abundance assessed by template matching in DYNAMO and subtomogram averaging in RELION 4.0 on a subset of data. Following successful reconstruction, the resulting density maps were used as templates for template matching on the full datasets. Curated particle coordinates were then input into DEEPFINDER for deep-learning–based particle detection to improve accuracy and coverage. The combined datasets from both approaches were refined in RELION 4.0 and M to generate final density maps and particle orientations for downstream analyses. (**B–G**) Classification steps for the mitochondrial ribosome and mHsp60 complexes during initial screening. To detect the presence of various mHsp60 complexes, the single-particle cryo-EM density map of a human mHsp60:mHsp10 football complex (EMDB 9195) was masked to generate references of the different complexes for initial classification. Upon masking, the reference maps were then low-pass filtered to 60 Å (B) or 40 Å (C-G) resolution and rescaled to 18.5 Å (B) or 9.25 Å (C-G) pixel size, to match the dimensions of the tomogram in the respective binning. All classification steps were performed without imposing symmetry. Abbreviations: C1 sym, C1 symmetry; LP filt, low-pass filtered; TM, template matching.

Figure S3

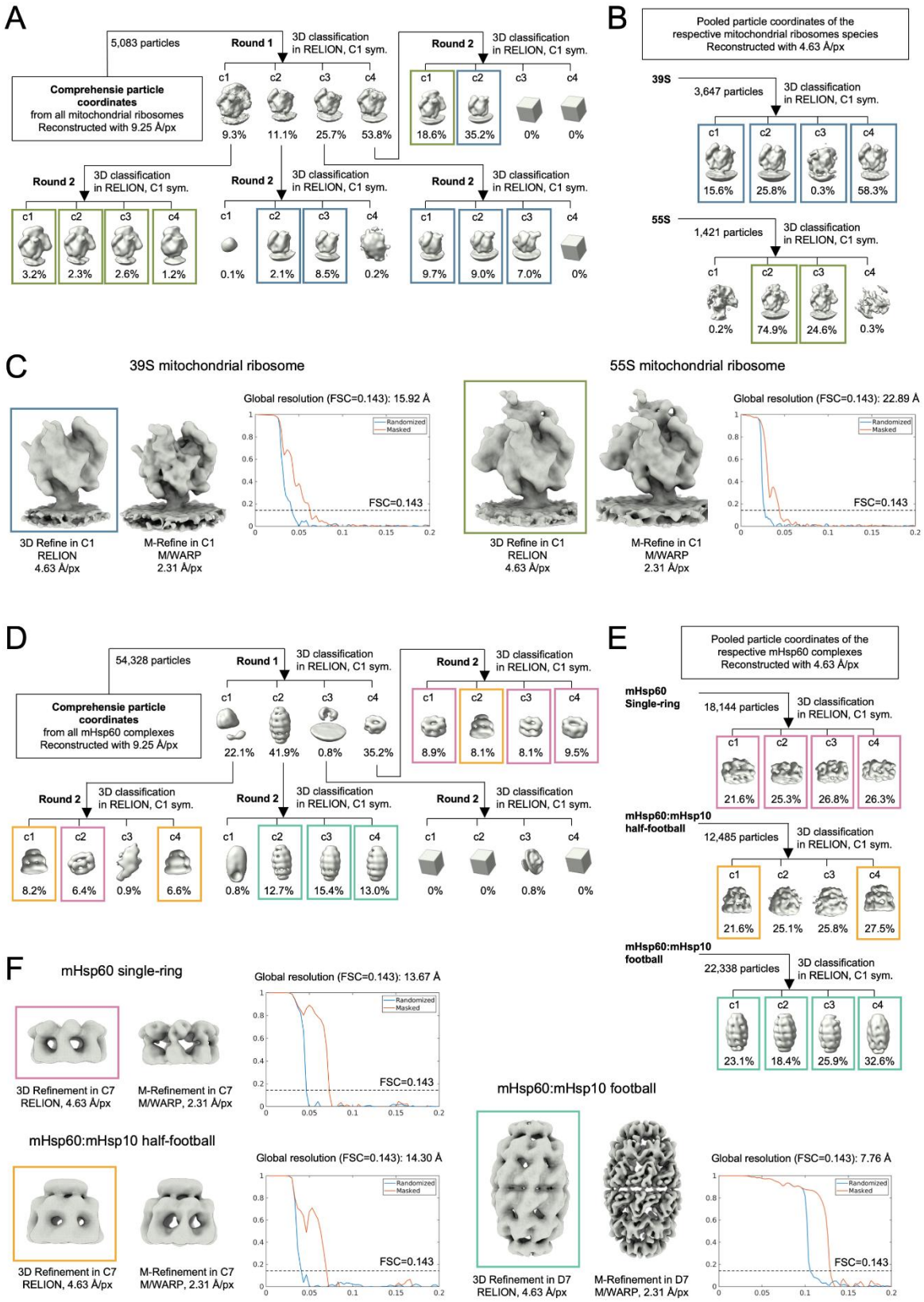
A
5,083 particles
Comprehensie particle coordinates
from all mitochondrial ribosomes
Reconstructed with 9.25 Å/px
Round 1
3D classification in RELION, C1 sym.
c1 c2 c3 c4
9.3% 11.1% 25.7% 53.8%
Round 2
3D classification in RELION, C1 sym.
c1 c2 c3 c4
18.6% 35.2% 0% 0%
Round 2
3D classification in RELION, C1 sym.
c1 c2 c3 c4
3.2% 2.3% 2.6% 1.2%
Round 2
3D classification in RELION, C1 sym.
c1 c2 c3 c4
0.1% 2.1% 8.5% 0.2%
Round 2
3D classification in RELION, C1 sym.
c1 c2 c3 c4
9.7% 9.0% 7.0% 0%
B
Pooled particle coordinates of the respective mitochondrial ribosomes species
Reconstructed with 4.63 Å/px
39S
3,647 particles
3D classification in RELION, C1 sym.
c1 c2 c3 c4
15.6% 25.8% 0.3% 58.3%
55S
1,421 particles
3D classification in RELION, C1 sym.
c1 c2 c3 c4
0.2% 74.9% 24.6% 0.3%
C
39S mitochondrial ribosome
Global resolution (FSC=0.143): 15.92 Å
Randomized
Masked
FSC=0.143
3D Refine in C1
RELION
4.63 Å/px
M-Refine in C1
M/WARP
2.31 Å/px
55S mitochondrial ribosome
Global resolution (FSC=0.143): 22.89 Å
Randomized
Masked
FSC=0.143
3D Refine in C1
RELION
4.63 Å/px
M-Refine in C1
M/WARP
2.31 Å/px
D
54,328 particles
Comprehensie particle coordinates
from all mHsp60 complexes
Reconstructed with 9.25 Å/px
Round 1
3D classification in RELION, C1 sym.
c1 c2 c3 c4
22.1% 41.9% 0.8% 35.2%
Round 2
3D classification in RELION, C1 sym.
c1 c2 c3 c4
8.9% 8.1% 8.1% 9.5%
Round 2
3D classification in RELION, C1 sym.
c1 c2 c3 c4
8.2% 6.4% 0.9% 6.6%
Round 2
3D classification in RELION, C1 sym.
c1 c2 c3 c4
0.8% 12.7% 15.4% 13.0%
Round 2
3D classification in RELION, C1 sym.
c1 c2 c3 c4
0% 0% 0.8% 0%
E
Pooled particle coordinates of the respective mHsp60 complexes
Reconstructed with 4.63 Å/px
mHsp60 Single-ring
18,144 particles
3D classification in RELION, C1 sym.
c1 c2 c3 c4
21.6% 25.3% 26.8% 26.3%
mHsp60:mHsp10 half-football
12,485 particles
3D classification in RELION, C1 sym.
c1 c2 c3 c4
21.6% 25.1% 25.8% 27.5%
mHsp60:mHsp10 football
22,338 particles
3D classification in RELION, C1 sym.
c1 c2 c3 c4
23.1% 18.4% 25.9% 32.6%
F
mHsp60 single-ring
Global resolution (FSC=0.143): 13.67 Å
Randomized
Masked
FSC=0.143
3D Refinement in C7
RELION, 4.63 Å/px
M-Refinement in C7
M/WARP, 2.31 Å/px
mHsp60:mHsp10 half-football
Global resolution (FSC=0.143): 14.30 Å
Randomized
Masked
FSC=0.143
3D Refinement in C7
RELION, 4.63 Å/px
M-Refinement in C7
M/WARP, 2.31 Å/px
mHsp60:mHsp10 football
Global resolution (FSC=0.143): 7.76 Å
Randomized
Masked
FSC=0.143
3D Refinement in D7
RELION, 4.63 Å/px
M-Refinement in D7
M/WARP, 2.31 Å/px

Figure S 3: *In situ* structural determination of mitochondrial ribosomes and mHsp60 complexes. (**A, D**) Curated and distance-filtered particle coordinates for mitochondrial ribosomes (A) and mHsp60 complexes (D). Particles were pooled and reclassified at bin 4 to identify the different assemblies. (**B, E**) Each assembly was further classified at bin 2 to remove remaining false positives and obtain the final particle sets used for refinement. (**C, F**) Final subtomogram averaging density maps were obtained after refinement at bin 2 in RELION 4.0, followed by multi-particle refinement at bin 1 using M. Abbreviations: C1 sym, C1 symmetry; FSC, Fourier shell correlation; px, pixel.

Figure S4

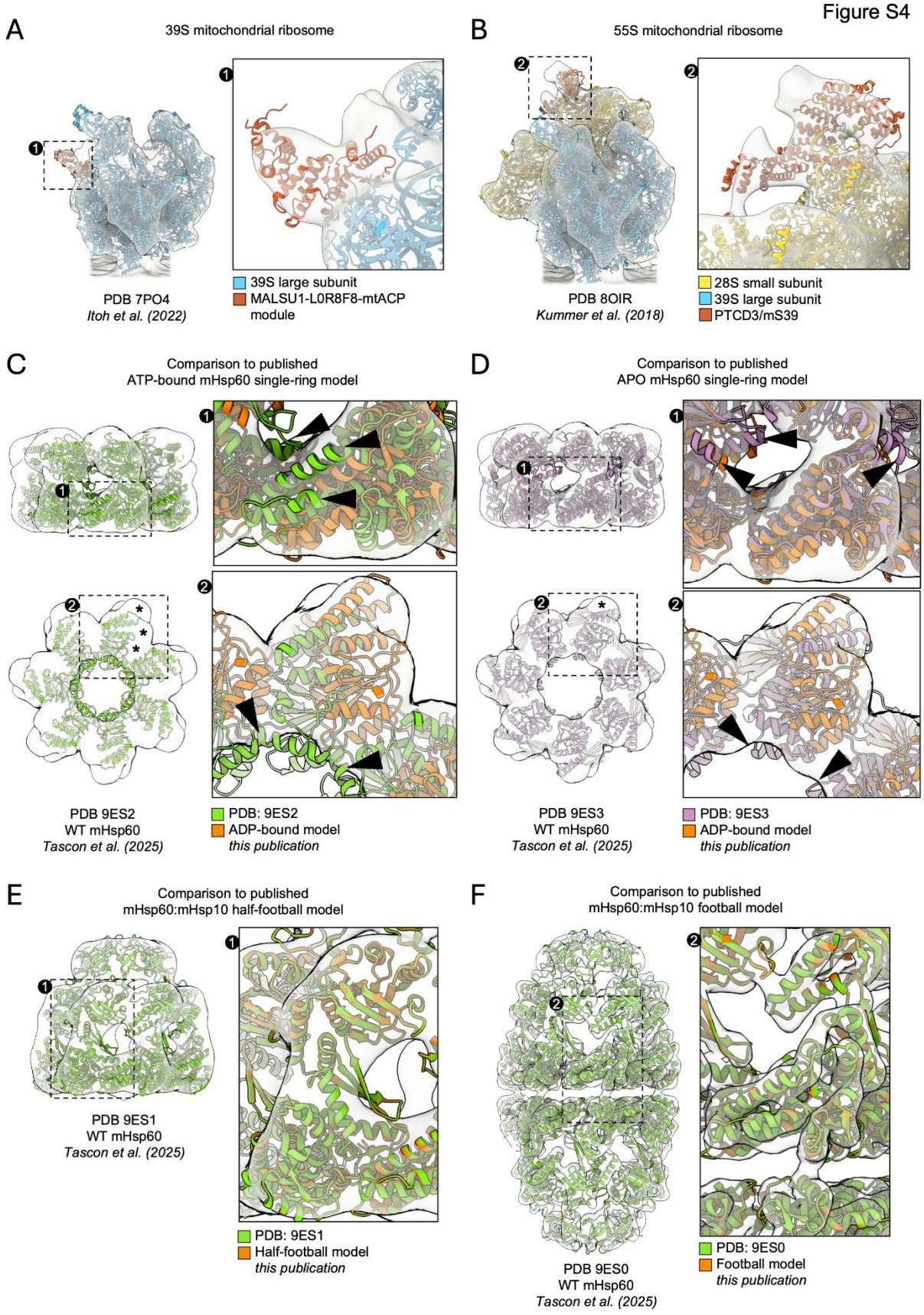
A
39S mitochondrial ribosome
PDB 7PO4
Itoh et al. (2022)
39S large subunit
MALSU1-L0R8F8-mtACP module
B
55S mitochondrial ribosome
PDB 8OIR
Kummer et al. (2018)
28S small subunit
39S large subunit
PTCD3/mS39
C
Comparison to published ATP-bound mHsp60 single-ring model
PDB 9ES2
WT mHsp60
Tascon et al. (2025)
PDB: 9ES2
ADP-bound model
this publication
D
Comparison to published APO mHsp60 single-ring model
PDB 9ES3
WT mHsp60
Tascon et al. (2025)
PDB: 9ES3
ADP-bound model
this publication
E
Comparison to published mHsp60:mHsp10 half-football model
PDB 9ES1
WT mHsp60
Tascon et al. (2025)
PDB: 9ES1
Half-football model
this publication
F
Comparison to published mHsp60:mHsp10 football model
PDB 9ES0
WT mHsp60
Tascon et al. (2025)
PDB: 9ES0
Football model
this publication

Figure S 4: Docking of atomic models into subtomogram averaging density maps. In all cases, *in situ* subtomogram averaging map are shown semitransparent. (**A**) Docking of the atomic model of a 39S mitochondrial ribosome assembly intermediate (PDB 7PO4). The inset highlights density consistent with the binding of the MALSU1–L0R8F8–mtACP module (Hillen *et al*, 2021; Lavdovskaia *et al*, 2024; Rebelo-Guiomar *et al*, 2022). (**B**) Docking of the atomic model of a fully assembled 55S mitochondrial ribosome (PDB 8OIR). The inset indicates density consistent with the binding of the RNA-binding and translation-regulating PTCD3/mS39 subunit (Kummer *et al*, 2018). (**C–F**) Docking of atomic models of WT mHsp60 complexes derived from single-particle cryo-EM into subtomogram averaging maps determined *in situ* using cryo-ET. We compare the cryo-EM structures determined in this study (orange) with published structures of mHSp60 complexes (green, purple). For clarity, comparisons are only shown with structures from (Tascon *et al*, 2025), which are representative of most other published mHps60 structures (Table S 1). (C, D) Comparison of the fit into subtomogram maps of ATP-bound (C) and apo (D) mHsp60 single-ring structures against ADP-bound mHsp60. Regions where the docked ATP and apo structures do not fit well the subtomogram density map are indicated by black arrowheads (structures extending beyond the map) and stars (densities in the map unaccounted for by the structures). (E, F) Overlays of published mHsp60:mHsp10 structures indicate only minimal variations compared to the ones determined in this study.

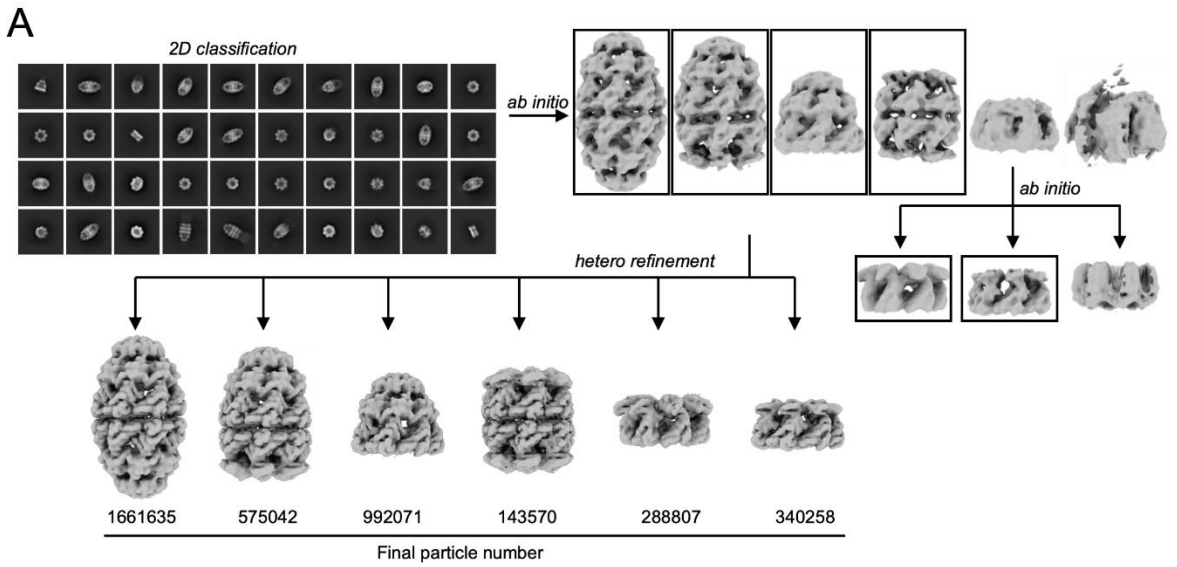
A
2D classification
ab initio
ab initio
hetero refinement
1661635
575042
992071
143570
288807
340258
Final particle number

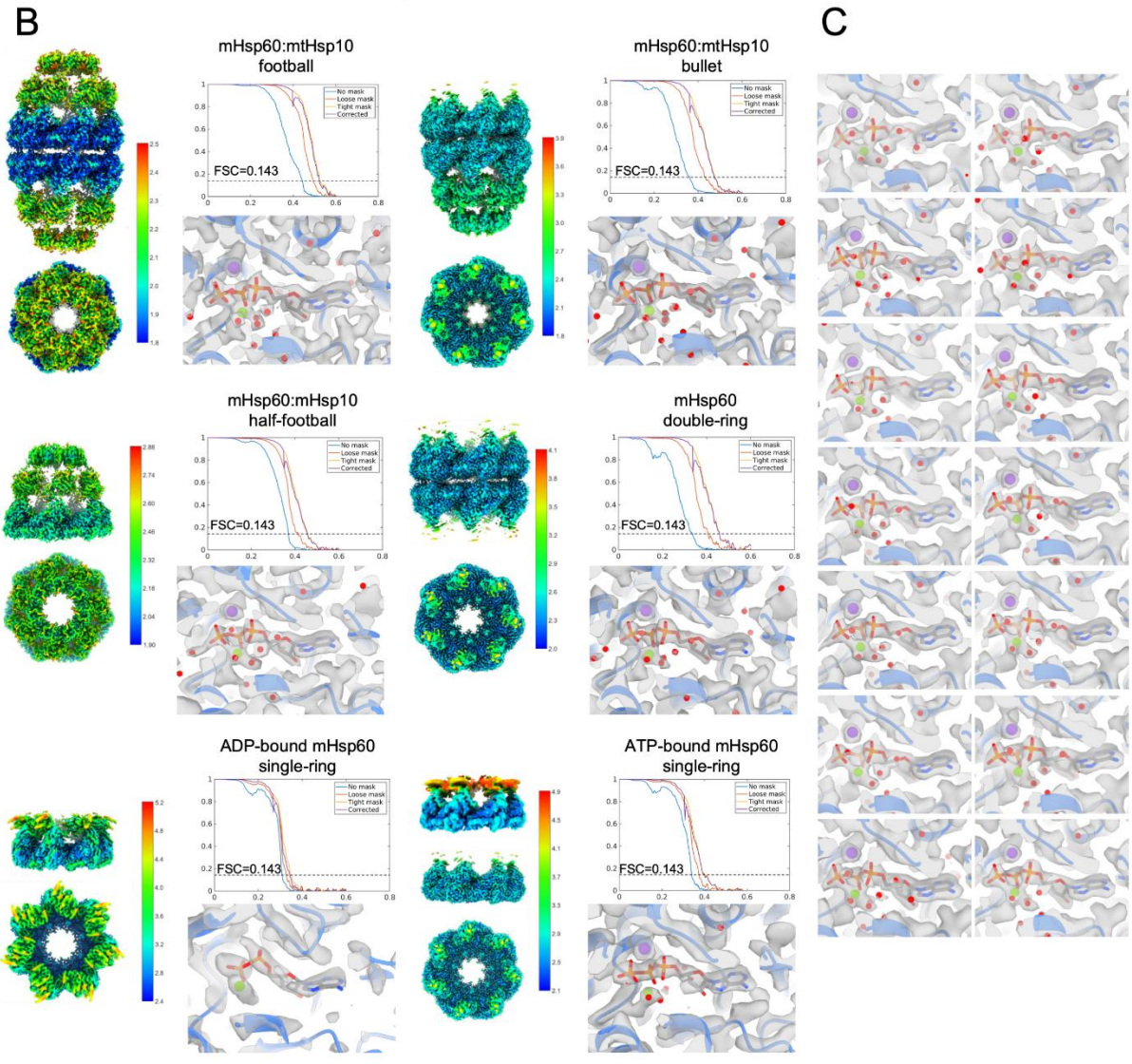
B
mHsp60:mtHsp10
football
mHsp60:mtHsp10
bullet
mHsp60:mtHsp10
half-football
mHsp60
double-ring
ADP-bound mHsp60
single-ring
ATP-bound mHsp60
single-ring
FSC=0.143
No mask
Loose mask
Tight mask
Corrected
C

Figure S 5: Structures of mHsp60 complexes determined *in vitro* by single-particle cryo-EM. (**A**) Cryo-EM data processing workflow for mHsp60 complexes. All datasets were processed independently, starting with particle picking, iterative 2D classification, and *ab initio* reconstruction. An additional *ab initio* reconstruction was performed specifically for particles contributing to single-ring classes. Boxes mark the *ab initio* volumes used for heterogeneous refinement. (**B**) Cryo-EM maps of ATP-bound mHsp60:mHsp10 football (1.92 Å nominal resolution), ATP-bound mHsp60:mHsp10 half-football (2.19 Å nominal resolution), ATP-bound mHsp60:mHsp10 bullet (2.1 Å nominal resolution), ADP-bound mHsp60 single-ring (2.91 Å nominal resolution), ATP-bound mHsp60 double ring (2.18 Å nominal resolution), and ATP-bound mHsp60 single-ring (2.50 Å nominal resolution) colored as a function of local resolution displayed as side and top views. FSC curves and detailed views of the nucleotide-binding sites for each species are also shown, displaying overlays of the density map (semitransparent) fitted with atomic models. The protein is depicted as blue ribbon, nucleotides as sticks, and Mg^{2+} ions (green), K^{+} ions (purple) and water molecules (red) as spheres. Cryo-EM maps were refined with D7 symmetry for the football and double-ring complexes, and C7 symmetry for the half-football, bullet, single-ring assemblies. For the ATP-bound mHsp60 single-ring, the map is also shown upon gaussian-filtering (top) to enable visualization of the highly-dynamic apical domains. (**C**) Nucleotide-binding sites of all 14 subunits of the ATP-bound mHsp60:mHsp10 football complex obtained by refinement without imposing symmetry (C1 symmetry). Abbreviations: FSC, Fourier shell correlation.

Figure S6

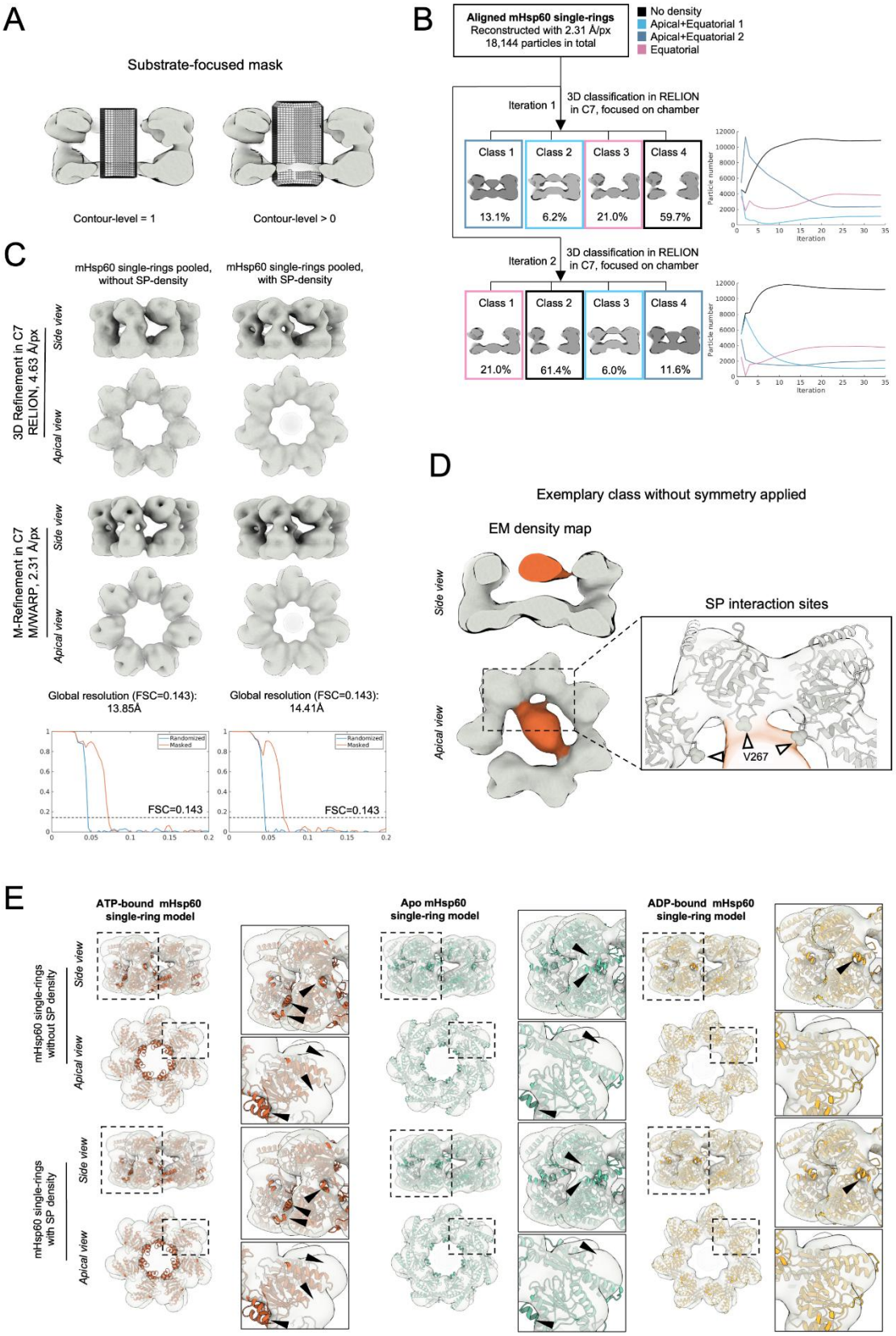
A
Substrate-focused mask
Contour-level = 1
Contour-level > 0
B
Aligned mHsp60 single-rings
Reconstructed with 2.31 Å/px
18,144 particles in total
No density
Apical+Equatorial 1
Apical+Equatorial 2
Equatorial
Iteration 1
3D classification in RELION
in C7, focused on chamber
Class 1
Class 2
Class 3
Class 4
13.1%
6.2%
21.0%
59.7%
Particle number
Iteration
Iteration 2
3D classification in RELION
in C7, focused on chamber
21.0%
61.4%
6.0%
11.6%
C
mHsp60 single-rings pooled,
without SP-density
mHsp60 single-rings pooled,
with SP-density
3D Refinement in C7
RELION, 4.63 Å/px
M-Refinement in C7
M/WARP, 2.31 Å/px
Side view
Apical view
Global resolution (FSC=0.143):
13.85Å
Global resolution (FSC=0.143):
14.41Å
Randomized
Masked
FSC=0.143
D
Exemplary class without symmetry applied
EM density map
SP interaction sites
V267
E
ATP-bound mHsp60
single-ring model
Apo mHsp60
single-ring model
ADP-bound mHsp60
single-ring model
mHsp60 single-rings
without SP density
mHsp60 single-rings
with SP density

Figure S 6: Substrate protein classification in mHsp60 single-ring complexes. (**A**) Mask of the central cavity used for focused 3D classification shown at different contour levels. The rendering at contour level = 1 represents the mask without the soft edge, while levels >0 visualize the full extent of the mask including the soft-edged boundary. (**B**) Classification results (left) and class occupancies over classification iterations (right) for two independent runs. (**C**) Independent refinements of the “No density” class versus SP-bound classes to assess potential structural differences. (**D**) Exemplary SP-bound class obtained from focused chamber-focused 3D classification in C1. The inset highlights the interactions between the SP density and V267 residues of mHsp60 (shown as spheres and marked by white arrowheads), as also observed in the classification using C7 symmetry (Figure 5B). (**E**) Docking of mHsp60 single-ring atomic models in different nucleotide states into the final subtomogram averaging maps from (C). Insets show magnified regions of interest, with black arrowheads indicating discrepancies between the model and the density map. Abbreviations: FSC, Fourier shell correlation; px, pixel.

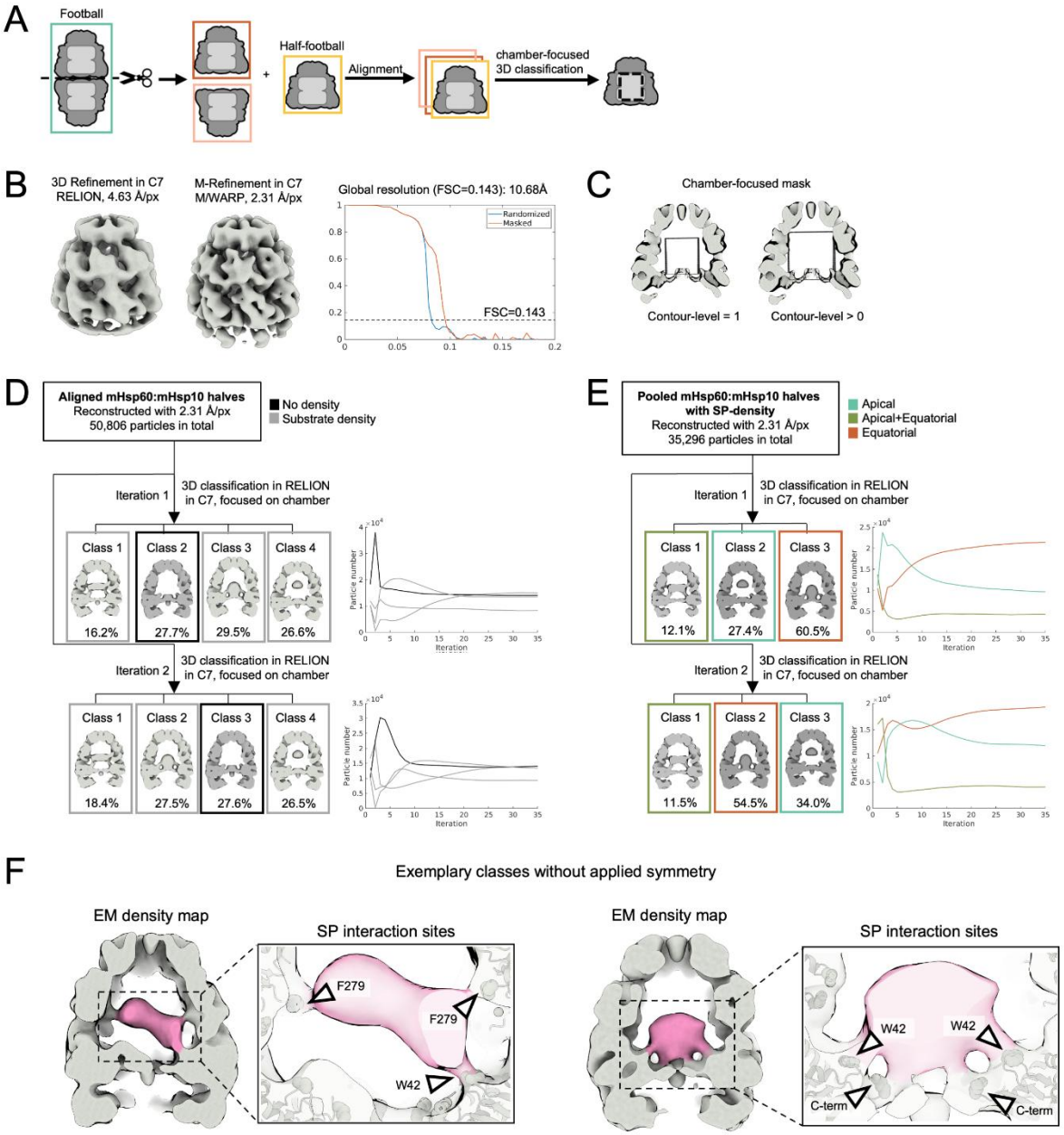

Figure S 7: Substrate protein classification in mHsp60:mHsp10 complexes. (**A**) Schematic overview of the processing workflow. mHsp60:mHsp10 football complexes were computationally bisected and their halves were aligned to *bona fide* mHsp60:mHsp10 half-football complexes prior to classification. (**B**) Refinement results for pooled mHsp60:mHsp10 half-maps including both *bona fide* mHsp60:mHsp10 half-footballs and bisected footballs. (**C**) Mask of the central cavity at different contour levels used for focused 3D classification. The rendering at contour level = 1

represents the mask without the soft edge, while levels >0 visualize the full extent of the mask including the soft-edged boundary. (**D**) First round of classification identifying empty chambers. Class averages (left) and class occupancies across iterations (right) are shown for two independent runs. (**E**) Second round of classification identifying different SP localization patterns. Class averages (left) and class occupancies across iterations (right) shown for two independent runs. (**F**) Examples of two different SP-bound classes obtained via focused 3D classification in C1. Insets highlight mHsp60 residues interacting with SPs are shown as spheres and indicated by arrowheads. These interaction sites were also identified using classification with applied symmetry (Figure 6B).

Table S 1: RMSD comparison between published single-particle cryo-EM structures of mHsp60 complexes and those determined in this study. Calculations were performed using the Matchmaker tool within ChimeraX (Goddard *et al*, 2018). The structures of WT mHsp60 complexes recently published by (Tascon *et al.*, 2025) were used as reference (9ES0, 9ES1, 9ES2, 9ES3). Only one ring of the ATP-bound mHsp60 double ring 9ES2 model was used for the calculations. The following structures of the V72I mHsp60 mutant were published by (Braxton *et al*, 2024): 8G7N (ATP-bound football), 8G7O (ATP-bound half-football), 8G7M (ATP-bound single-ring) and 8G7K (apo single-ring). The following structures of WT mHsp60 were published by (Gomez-Llorente *et al*, 2020): 6MRC (ADP-bound football), 6MRD (ADP-bound half-football). The 7AZP of WT mHsp60 apo single ring was published by (Klebl *et al*, 2021). The 7L7S of WT mHsp60 apo single ring was published by (Wang & Chen, 2021).

Reference model	Matching model	RMSD (all pairs)
9ES0 (ATP football) (Tascon et al., 2025)	ATP football (this study)	0.250 Å
	8G7N	0.729 Å
	6MRC	0.471 Å
9ES1 (ATP half-football) (Tascon et al., 2025)	ATP half-football (this study)	0.324 Å
	8G7O	0.780 Å
	6MRD	0.642 Å
9ES2 (ATP double-ring) (Tascon et al., 2025)	ATP single-ring (this study)	0.816 Å
	ADP single-ring (this study)	2.658 Å
	8G7M	2.844 Å
9ES3 (Apo single-ring) (Tascon et al., 2025)	ATP single-ring (this study)	3.883 Å
	ADP single-ring (this study)	7.289 Å
	8G7K	1.327 Å
	7AZP	0.545 Å
	7L7S	1.036 Å

Table S 2: **Cryo-EM data collection, refinement and validation statistics**

	ATP-bound $mHsp60_{14}$-$mHsp10_{14}$ (EMDB 54898) (PDB 9SHG)	ATP-bound $mHsp60_{14}$-$mHsp10_{7}$ (EMDB 54899) (PDB 9SHH)	ATP-bound $mHsp60_{7}$-$mHsp10_{7}$ (EMDB 54990) (PDB 9SHI)
Data collection and processing			
Magnification	105000	105000	105000
Voltage (kV)	300	300	300
Electron exposure (e–/Å^2)	50	50	50
Defocus range (μm)	0.8-1.6	0.8-1.6	0.8-1.6
Pixel size (Å)	0.8238	0.8238	0.8238
Symmetry imposed	D7	C7	D7
Initial particle images (no.)	12338206	12338206	12338206
Final particle images (no.)	1661635	575042	992071
Map resolution (Å)	1.91	2.11	2.19
FSC threshold	0.143	0.143	0.143
Map resolution range (Å)	1.845 - 20.712	1.881 - 30.220	1.818 - 25.245
Refinement			
Initial model used (PDB code)	9ES0	9ES1/9ES2	9ES1
Model resolution (Å)	2.0	2.2	2.5
FSC threshold	0.5	0.5	0.5
Map sharpening *B* factor (Å^2)	-60.4	-60.3	-75.5
Model composition			
Non-hydrogen atoms	68854	63040	34531
Protein residues	8778	8078	4389
Ligands	42	42	21
B factors (Å^2)			
Protein	43.14	69.33	47.69
Ligand	11.32	17.88	18.59
R.m.s. deviations			
Bond lengths (Å)	0.004	0.004	0.004
Bond angles (°)	0.680	0.676	0.636
Validation			
MolProbity score	1.05	1.20	1.10
Clashscore	2.65	4.21	3.13
Poor rotamers (%)	0.00	0.00	0.00
Ramachandran plot			
Favored (%)	98.73	98.36	98.62
Allowed (%)	1.27	1.64	1.38
Disallowed (%)	0.00	0.00	0.00

	ATP-bound $mHsp60_{14}$ (EMDB 54991) (PDB 9SHJ)	ADP-bound $mHsp60_{7}$ (EMDB 54992) (PDB 9SHK)	ATP-bound $mHsp60_{7}$ (EMDB 54993) (PDB 9SHGL)
Data collection and processing			
Magnification	105000	105000	105000
Voltage (kV)	300	300	300
Electron exposure (e–/Å^2)	50	50	50
Defocus range (μm)	0.8-1.6	0.8-1.6	0.8-1.6
Pixel size (Å)	0.8238	0.8238	0.8238
Symmetry imposed	D7	C7	C7
Initial particle images (no.)	12338206	12338206	12338206
Final particle images (no.)	143570	288807	340258
Map resolution (Å)	2.18	2.91	2.50
FSC threshold	0.143	0.143	0.143
Map resolution range (Å)	1.978 - 34.455	1.768 - 9.351	2.147 - 24.030
Refinement			
Initial model used (PDB code)	9ES2	9ES1	9ES2
Model resolution (Å)	2.3	3.3	2.8
FSC threshold	0.5	0.5	0.5
Map sharpening *B* factor (Å^2)	-58.0	-106.0	-97.6
Model composition			
Non-hydrogen atoms	56446	27629	28015
Protein residues	7378	3682	3689
Ligands	42	14	21
B factors (Å^2)			
Protein	101.83	9.31	72.59
Ligand	23.53	2.57	11.03
R.m.s. deviations			
Bond lengths (Å)	0.003	0.004	0.004
Bond angles (°)	0.597	0.668	0.659
Validation			
MolProbity score	1.25	1.64	1.38
Clashscore	4.76	10.15	5.69
Poor rotamers (%)	0.00	0.00	0.00
Ramachandran plot			
Favored (%)	98.19	97.44	97.66
Allowed (%)	1.81	2.56	2.34
Disallowed (%)	0.00	0.00	0.00

References

Braxton JR, Shao H, Tse E, Gestwicki JE, Southworth DR (2024) Asymmetric apical domain states of mitochondrial hsp60 coordinate substrate engagement and chaperonin assembly. *Nat Struct Mol Biol* 31: 1848-1858. doi: 10.1038/s41594-024-01352-0

Goddard TD, Huang CC, Meng EC, Pettersen EF, Couch GS, Morris JH, Ferrin TE (2018) Ucsf chimerax: Meeting modern challenges in visualization and analysis. *Protein Sci* 27: 14-25. doi: 10.1002/pro.3235

Gomez-Llorente Y, Jebara F, Patra M, Malik R, Nisemblat S, Chomsky-Hecht O, Parnas A, Azem A, Hirsch JA, Ubarretxena-Belandia I (2020) Structural basis for active single and double ring complexes in human mitochondrial hsp60-hsp10 chaperonin. *Nat Commun* 11: 1916. doi: 10.1038/s41467-020-15698-8

Hillen HS, Lavdovskaia E, Nadler F, Hanitsch E, Linden A, Bohnsack KE, Urlaub H, Richter-Dennerlein R (2021) Structural basis of gtpase-mediated mitochondrial ribosome biogenesis and recycling. *Nat Commun* 12: 3672. doi: 10.1038/s41467-021-23702-y

Klebl DP, Feasey MC, Hesketh EL, Ranson NA, Wurdak H, Sobott F, Bon RS, Muench SP (2021) Cryo-em structure of human mitochondrial hspd1. *iScience* 24: 102022. doi: 10.1016/j.isci.2020.102022

Kummer E, Leibundgut M, Rackham O, Lee RG, Boehringer D, Filipovska A, Ban N (2018) Unique features of mammalian mitochondrial translation initiation revealed by cryo-em. *Nature* 560: 263-267. doi: 10.1038/s41586-018-0373-y

Lavdovskaia E, Hanitsch E, Linden A, Pasen M, Challa V, Horokhovskyi Y, Roetschke HP, Nadler F, Welp L, Steube E *et al* (2024) A roadmap for ribosome assembly in human mitochondria. *Nat Struct Mol Biol* 31: 1898-1908. doi: 10.1038/s41594-024-01356-w

Rebelo-Guiomar P, Pellegrino S, Dent KC, Sas-Chen A, Miller-Fleming L, Garone C, Van Haute L, Rogan JF, Dinan A, Firth AE *et al* (2022) A late-stage assembly checkpoint of the human mitochondrial ribosome large subunit. *Nat Commun* 13: 929. doi: 10.1038/s41467-022-28503-5

Tascon I, Lopez-Alonso JP, Shkolnisky Y, Gil-Carton D, Vilchez-Garcia J, Berruezo AG, Gomez-Llorente Y, Malik R, Jebara F, Patra M *et al* (2025) Structural basis for atp-driven double-ring assembly of the human mitochondrial hsp60 chaperonin. *bioRxiv*: 2025.2010.2004.680452. doi: 10.1101/2025.10.04.680452

Wang JC, Chen L (2021) Structural basis for the structural dynamics of human mitochondrial chaperonin mhsp60. *Scientific reports* 11: 14809. doi: 10.1038/s41598-021-94236-y